

Atomic-Scale Mechanism of Unidirectional Oxide Growth

*Xianhu Sun, Wenhui Zhu, Dongxiang Wu, Zhenyu Liu, Xiaobo Chen, Lu Yuan, Guofeng Wang,
Renu Sharma, Guangwen Zhou**

X. H. Sun, Dr. W. H. Zhu, D. X. Wu, X. B. Chen, Dr. L. Yuan, Prof. G. W. Zhou

Department of Mechanical Engineering & Materials Science and Engineering Program, State
University of New York, Binghamton, NY 13902, USA

E-mail: gzhou@binghamton.edu

Dr. Z. Y. Liu, Prof. G. F. Wang

Department of Mechanical Engineering and Materials Science, University of Pittsburgh,
Pittsburgh, Pennsylvania 15261, USA

Dr. R. Sharma

Physical Measurement Laboratory, National Institute of Standards and Technology, Gaithersburg,
MD 20899, USA

Keywords: oxidation, copper, CuO nanowire, grain boundary diffusion, environmental
transmission electron microscopy

A fundamental knowledge of the unidirectional growth mechanisms is required for precise control on size, shape, and thereby functionalities of nanostructures. The oxidation of many metals results in oxide nanowire growth with a bicrystal grain boundary along the axial direction. Using transmission electron microscopy that spatially and temporally resolves CuO nanowire growth during the oxidation of copper, here we provide direct evidence of the correlation between unidirectional crystal growth and bicrystal grain boundary diffusion. Based on atomic scale observations of the upward growth at the nanowire tip, oscillatory downward growth of atomic layers on the nanowire sidewall and the parabolic kinetics of lengthening, bicrystal grain boundary diffusion is the mechanism by which Cu ions are delivered from the nanowire root to the tip. Together with density-functional theory calculations, we further show that the asymmetry in the corner-crossing barriers promotes the unidirectional oxide growth by hindering the transport of Cu ions from the nanowire tip to the sidewall facets. We expect the broader applicability of these results in manipulating the growth of nanostructured oxides by controlling the bicrystal grain boundary structure that favors anisotropic diffusion for unidirectional, one-dimensional crystal growth for nanowires or isotropic diffusion for two-dimensional platelet growth.

1. Introduction

More than 70 % of the elements in the periodic table are metals, signifying that a wealth of metal oxides with various properties and functionalities could be fabricated. Particularly, oxide nanowires represent an important class of quasi-one-dimensional (1D) nanomaterials and have received broad interest because of the possibility of tuning their functionalities by size, shape, stoichiometry, phase, atomic termination and defects. Moreover, oxidation induced oxide nanowire formation has received considerable attention for its technical simplicity and large-scale growth possibility with high crystalline quality.^[1] Contrary to its technical simplicity, however, the mechanism underlying the oxide nanowire growth has not been resolved to date although the oxide whisker formation during the oxidation of metals was observed frequently back in 1950s.^[2] Precise nanocrystal growth with controlled size, shape, and functionalities requires a fundamental knowledge of the growth mechanism, thereby allowing manipulation of the growth process. Growth kinetics plays a key role in controlling the morphology, shape, and facets of nanocrystals.^[2e, 3] In bulk or ensemble systems, crystal growth proceeds through the nucleation and growth processes and the kinetic understanding is developed around the statistical averaging of these two convoluted processes. Thus, many key aspects of the crystal growth may be buried in these entangled events and cannot be resolved directly. Among the leading challenges is the ability to disentangle these events via visualizing complex growth processes under *in situ* conditions.

Transmission electron microscopy (TEM) has evolved dramatically in recent years and the development of environmental TEM enables disentangling nucleation and growth kinetics through atomically resolved imaging of the dynamic evolution of the local atomic configurations at the vapor-solid and solid-solid interfaces.^[4] By employing a dedicated environmental TEM

equipped with an image corrector and a differential pumping system, here we report *in situ* TEM visualization of the growth of oxide nanowires during the oxidation of copper, which provides significant new insight into the rather complex kinetic process underlying the directional crystal growth. By introducing reactive gases into the sample region while simultaneously monitoring the structure changes at the atomic scale, we monitor the growth of individual CuO nanowires by directly imaging the nucleation and growth of atomic layers at the growing end of CuO nanowires formed by heating metallic Cu in an O₂ gas flow. Here, we describe a nanowire growth phenomenon, driven by axial bicrystal grain boundary diffusion along the length of the nanowire. The self-propagation of atomic steps at the nanowire tip with adatoms supplied through the bi-crystal grain boundary diffusion enables one-dimensional crystal growth. The dynamic visualization of the oxide growth at the atomic scale demonstrates the remarkable ability of bi-crystal grain boundaries to direct the unidirectional growth of crystals.

2. Results and Discussion

Two thermodynamically stable oxides of Cu, Cu₂O and CuO, form upon the oxidation of Cu by O₂. **Figure 1(a)** is a scanning electron microscopy (SEM) image showing the cross-sectional morphology of an oxidized Cu substrate after oxidation at T=400 °C and 2.67×10⁴ Pa of the oxygen pressure (pO₂). The bi-layer oxide structure visible in Figure 1(a) can be identified as the Cu₂O layer next to the Cu substrate and the CuO layer on top, based on X-ray energy dispersive spectroscopy (EDS) composition analysis with the O/Cu atomic ratio ≈ 0.9 for the outer layer, ≈ 0.45 for the middle layer, and ≈ 0 in the bottom layer, in agreement with the previous studies.^[3b, 5] Such oxide layering is governed by the Cu to O₂ phase equilibria with the stability of CuO > Cu₂O and the oxygen chemical potential gradient across the oxide layers due

to many orders of magnitude in the oxygen chemical potential difference between the O_2/CuO and the buried CuO/Cu_2O interfaces.^[6] CuO growth takes place at the O_2/CuO interface because the large oxygen chemical potential surrounding the outer surface favors the CuO formation. Compared to the O_2/CuO interface, there is a significant drop in the oxygen pressure at the buried CuO/Cu_2O interface, for which the Cu_2O formation is more favorable at the CuO/Cu_2O interface. Therefore, the inner portion of the oxygen-rich CuO layer undergoes decomposition and transforms to Cu_2O at the CuO/Cu_2O interface, which results in the thickening of the intermediate Cu_2O layer. Such CuO/Cu_2O bilayer oxide growth produces Cu vacancies and electron holes at the O_2/CuO and CuO/Cu_2O interfaces, which migrate through the CuO and Cu_2O layers, being annihilated finally at the Cu_2O/Cu interface, accompanied by the counter diffusion of Cu ions from the Cu_2O/Cu interface to the outer surface of the CuO layer.^[6-7]

In addition to the bilayer oxide growth, Figure 1(a) shows the formation of aligned CuO nanowire forest on the outer surface of the CuO layer. The CuO nanowires are relatively perpendicular to the CuO layer and have a relatively uniform diameter with the lengths up to tens of micrometers. The nanowire roots are buried by the CuO layer, as marked by white arrows in Figure 1(a). Figure 1(b) shows a TEM image of the typical morphology of single CuO nanowires, from which we can see that the nanowire has a diameter of ≈ 30 nm with a tapered shape at the tip. There is a sharp boundary along the middle from the bottom to the tip, indicating that the nanowire has a bicrystal grain boundary structure, as evidenced by the HRTEM image in Figure 1(c). The HRTEM image was recorded with the grain boundary plane in an edge-on position. A typical synthesis route for producing 1D structures involves exploiting the catalytic effect on directional crystal growth, where the catalyst particle at the nanowire tip serves as the active site that directs the incorporation of atoms segregated from a supersaturated liquid droplet to the

growing end of the nanowires.^[8] The low magnification TEM images as shown in Figure 1(b) confirm a lack of catalysts at the tips of the formed CuO nanowires, indicating the vapor-liquid-solid (VLS) mechanism does not apply to the oxidation-induced oxide whiskering. Instead, the presence of the bicrystal grain boundary extending through the entire length direction up to the tip points to its critical role in the unidirectional crystal growth. Indeed, bicrystal grain boundaries are widely observed in oxide nanowires formed from the oxidation of metals^[1e, 3b, 9] and the bicrystal grain boundary edge at the nanowire tip has been shown as the preferred sites for nucleating new atomic layers for the tip growth.^[10] However, the mass transport mechanism for leading to the unidirectional oxide growth from the oxidation of metals has been a long-standing controversial topic.^[3b, 11] As shown from *in situ* environmental TEM observations described below, here we provide real-time evidence of the mass transport mechanisms that combines two diffusion processes, where the nanowire tip growth is controlled by bicrystal grain boundary diffusion for the delivery of Cu ions from the nanowire root to the tip while the bottom-up surface diffusion along the nanowire sidewall results in the lateral growth, mostly at the root.

Environmental TEM is capable of introducing a gas phase into the sample region and thus allows for concurrent nanowire growth and continuous monitoring of the growth of individual nanowires, thereby providing real-time evidence of growth mechanisms.^[8d, 10, 12] Figure S1 in Supporting Information shows schematics of the experimental setup for *in situ* TEM observation of CuO nanowire growth during the oxidation of Cu, where the Cu substrate is resistively heated with the TEM specimen holder in an oxygen gas pressure of ≈ 0.5 Pa, maintained locally at the sample region using differentially pumped apertures. With this setup, we perform real-time low-magnification TEM imaging to monitor the length evolution of

individual CuO nanowires throughout the growth process and *in situ* high-resolution TEM (HRTEM) imaging of the atomic process of oxide growth at the tip and side facets of the nanowires. Due to the limitation by the TEM, the oxygen pressure used for our in-situ ETEM observations is much lower than that for the ex-situ oxidation experiments ($\approx 2.67 \times 10^4$ Pa) shown in Figure 1(a). Our TEM characterization has confirmed the Cu₂O and CuO formation in the in-situ TEM experiments, same as that from the ex-situ oxidation experiment at the higher pO₂. This is also consistent with the phase diagram of the copper-oxygen system that predicts the Cu₂O and CuO formation at 400°C with the oxygen pressure below ~ 0.001 Pa.^[13] Previous studies have shown that the length and diameter of CuO nanowires increase with increasing pO₂.^[14] As shown below, oxide nanowires formed from the oxidation at the low pO₂ share the same microstructure feature as those from the high pO₂ with the presence of a bicrystal grain boundary along the axial direction. This indicates the same diffusion mechanism for the oxide nanowire growth despite of oxygen pressure differences.

Figure 1(d-l) show a time sequence of *in situ* TEM snapshots captured from supporting TEM Movie 1 revealing growth of CuO nanowires on the CuO layer during the oxidation of a Cu substrate. As seen in Figure 1(d), a CuO nanowire (marked by the blue dashed line) sprouts from the base of a grain boundary groove. The nanowire grows and surpasses the surface height of the surrounding grains (Figure 1(e-h)). The yellow dashed rectangles in Figure 1(i-l) mark the growth of a second CuO nanowire from an adjacent region. It can be noted from Figure 1(d-l) that the CuO nanowires do not show the bicrystal grain boundary contrast as shown in Figure 1(b), this is because of the tilt of the grain boundary plane away from the incident electron beam.

Figure 1(m) illustrates the length evolution of the CuO nanowire versus growth time, t , measured from *in situ* TEM Movie 1.

For oxidation controlled by outward diffusion of metal ions at elevated temperature, the oxide growth obeys the parabolic law as predicted by the well-known Wagner's theory.^[6, 15] Previous work has shown that the rate-limiting step for the oxidation of Cu in the intermediate temperature range (< 500 °C) is outward grain boundary diffusion, which is essentially parabolic.^[3b, 7] As seen in Figure 1(d-l), the nanowire growth slows down as the nanowire increases in its length, suggesting that the nanowire length growth is controlled by a diffusion process, for which the increase in the nanowire length results in a longer diffusion distance for the transfer of Cu ions from the nanowire root to its tip. As shown in Figure 1(m), the time evolution of the nanowire length can be fitted well with the parabolic kinetics, suggesting that the oxide nanowire lengthening is controlled by the outward diffusion of Cu ions from the nanowire root through the bicrystal grain boundary within the nanowire to its tip, where the arriving Cu ions react with adsorbed oxygen from the gas phase to form new oxide layer, as observed directly by atomic-scale HRTEM imaging described later. As can be also noted from Figure 1(d-l), there is a slight increase in the diameter around the nanowire root, suggesting the lateral oxide growth resulting from the reaction of adsorbed oxygen with Cu ions supplied from the bottom-up sidewall diffusion. However, the long-distance upward sidewall diffusion of Cu ions to the nanowire tip is impeded because of the presence of readily available oxygen that results in the oxide formation in the root region. By contrast, Cu ions from the grain boundary diffusion are not consumed (due to the lack of additional oxygen) before reaching the nanowire tip, where they react with adsorbed oxygen to form new oxide. This is consistent with the parabolic kinetics of the nanowire lengthening (Figure 1(m)) that implies a conservative

diffusion flux along the bicrystal grain boundary with negligible contribution from the sidewall diffusion. In our TEM observations, careful oxidation experiments with and without electron beam irradiation were conducted to identify possible irradiation induced effect, and the results and analysis were drawn from various experiments conducted on different regions of various samples. The presence of bicrystal grain boundaries in the nanowires was observed in both cases, indicative of the same growth mechanism. The electron beam can result in slightly faster growth due to the irradiation effect on the dissociation of oxygen molecules, as shown in supporting Movies 1-3, and Figure S2. However, the parabolic kinetics is independent of the electron dose rates, confirming the negligible electron beam effect on the growth mechanism.

Figure 2 presents time sequence of HRTEM images (extracted from supporting Movie 4) illustrating the lengthening process of a CuO nanowire by nucleation and lateral propagation of atomic layers at the nanowire tip. As seen in Figure 2(a), the nanowire has a bicrystal grain boundary along the axis direction through the nanowire tip. The bicrystal plane is not exactly parallel to the viewing direction, which results in some projected width of the bicrystal plane in the middle region of the nanowire, as indicated by the two dashed lines in Figure 2(a). The bicrystal grain boundary intersects the nanowire tip with a terrace-step configuration at the tip, where the surface height of the right grain is higher than the left one by five ($1\bar{1}0$) atomic layers. Figure 2(b) shows schematically the terrace-step configuration of the nanowire tip. As seen from *in situ* TEM Movie 4 and the snapshots in Figure 2(c-1), there is continuously faster oxide formation local to the location of the grain boundary emergence to the nanowire tip, resulting in a small protrusion (as marked by the yellow arrows in Figure 2(c, d)). The constantly faster oxide growth at the site where the bicrystal grain boundary emerges serves as a strong indication of the ejection of a large flux of Cu ions through the bicrystal grain boundary diffusion, where the

reaction of ejected Cu ions with adsorbed O atoms from the surrounding oxygen results in the instant oxide formation of an island-like protrusion at the bicrystal grain boundary. By contrast, no such locally large protrusion is expected from the bottom-up surface diffusion of Cu ions via the nanowire sidewall because the sidewall diffusion should lead to the layer-by-layer, step flow growth (starting from the bicrystal grain boundary edge) rather than the overgrowth above the bicrystal grain boundary edge at the nanowire tip. The dynamic evolution of the oxide growth at the nanowire tip revealed from the *in situ* TEM observation provides compelling evidence that the Cu ions required for the oxide growth at the tip are supplied from the bicrystal grain boundary, that is, the bicrystal grain boundary diffusion provides the kinetic pathway that enables the transport of Cu ions from the nanowire root to the tip, as schematically illustrated by green arrows in Figure 2(b). It is worth mentioning that the supply of Cu ions by surface diffusion along the nanowire sidewall is unlikely for the observed growth behavior because the ready availability of oxygen in the surrounding results in the consumption of Cu ions on the outer surface before they reach the nanowire tip. This is in contrast to the upward grain boundary diffusion, for which Cu ions are not consumed to form new oxide before they reach the nanowire tip.

Besides the supply of Cu ions to the tip by bicrystal grain boundary diffusion, more microscopic detail of the nucleation and growth process of atomic planes at the nanowire tip is revealed from the *in situ* TEM observations. As shown in Figure 2(a, c-d), the formation of new atomic planes occurs preferentially on the lower terrace starting from the step-terrace corner and propagating laterally via step flow toward the left. Therefore, the surface height of the grain on the left grows faster and catches up with that of the grain on the right. The dashed green line in Figure 2(d) marks the surface height of the initial step-terrace configuration seen in Figure 2(a)

and shows that from 0 s to 35.4 s the left grain grows by seven $\text{CuO}(1\bar{1}0)$ atomic layers while only two $(1\bar{1}0)$ layers are formed on the terrace of the right grain. The step-flow growth of new atomic layers at the tip results from the increased coordination for Cu ions attaching to the step edges than staying on terraces. Therefore, the step edges facilitate the nucleation and growth of new atomic layers by acting as the effective trapping centers for mobile O and Cu ions. This also agrees with the previous study showing that the twin boundary edge is the preferential site for the oxide nucleation at the nanowire tip.^[10]

Meanwhile, nucleation and lateral growth of new $(1\bar{1}0)$ atomic planes can also take place at different locations of the tip upon the spreading of the Cu ions supplied from the bi-crystal boundary diffusion. Figure 2(e-h) show a time sequence of the nucleation and growth of a new CuO layer on the terrace, followed by the lateral propagation of the atomic layer by step-edge flow at the two ends of the nucleated atomic layer. This process repeats itself and Figure 2(i-l) show another event of nucleating a new $(1\bar{1}0)$ layer at the center of the terrace and the subsequent lateral growth by the step-edge flow at the two ends of the atomic layer. Figure 2(m-p) illustrate the nucleation of a new $(1\bar{1}0)$ layer in the right corner region of the tip, for which the growth is dominated by the flow of the step toward the left until reaching the bicrystal grain boundary. The step-flow growth of the oxide layers indicates that the nanowire tip grows via an adatom process by the surface diffusion of Cu ions that are delivered first to the nanowire tip through the bicrystal grain boundary diffusion.

Figure 3 shows atomic level details about the nanowire tip with the viewing direction perpendicular to the bicrystal plane. Figure 3(a) is an HRTEM image along the $[110]$ zone axis, which shows that the nanowire tip has a trapezoidal shape consisting of the terminated facets of

($1\bar{1}1$), ($1\bar{1}\bar{1}$) and ($1\bar{1}\bar{3}$), as identified from the diffractogram analysis (Figure 3(b)). A careful inspection of the HRTEM image in Figure 3(a) shows weak moiré fringe contrast, which is formed as a result of interference between diffracted beams from overlapping CuO grains. The overlapping of the bicrystal grains with respect to the viewing direction can be further confirmed from the feature shown in the small, extended narrow region in the lower right corner of the nanowire tip, marked by a red arrow in Figure 3(a), which corresponds to the protruding part of one of the crystals due to its larger width than the other crystal. This protruding region is out of focus compared to the other crystal and thus has reduced image contrast. From this viewing direction, it cannot be resolved readily whether the nanowire tip has a step-terrace configuration formed by two grains with different surface heights, as the nanowire tip shown in Figure 2. However, we still can conclude that the tip has a step-terrace configuration, as inferred from the absence of Moire contrast in the very top region of the tip.

Figure 3(c-n) depict *in situ* TEM observations of the nucleation and growth of atomic planes in the different regions of the nanowire tip marked in Figure 3(a). It is worth mentioning that the tip growth feature revealed from the in-situ TEM imaging shown in Figure 3 is always tied to the topmost surface of the taller grain. Figure 3(c-f) show time-sequence HRTEM snapshots (supporting *in situ* TEM Movie 5) captured from the top-left corner region of the growth tip as marked by the green dashed rectangle in Figure 3(a). As seen in Figure 3(c, d), a single atomic layer nucleates at the corner with the step-flow growth toward the right along the ($1\bar{1}1$) terrace. Figure 3(e, f) further show that the step-flow growth can involve a bilayer growth process, by which two atomic CuO layers grow simultaneously at the tip. Figure 3(g, h) illustrate the step-flow growth of multiple atomic layers in the middle region of the tip (see supporting *in*

situ TEM Movie 6). As shown in Figure 3(g), there are four atomic steps present at the tip, marked by the red and white arrows. The two atomic steps marked by the white arrows in Figure 3(g) grow out of the field of the TEM view in Figure 3(h), while the two steps marked by the yellow arrows propagate further toward the right and are still visible. Meanwhile, two new steps enter the field of the view, as marked by the two red arrows in Figure 3(h). Finally, these atomic steps propagate across the terrace and reach the tip corner on the right, thereby stopping their growth, as shown in Figure 3(i-j). The green dashed lines in Figure 3(i-j) outline surface profile trace of the tip at 3.3 s, which show that nanowire tip grows by four atomic layers at 7.3 s time stamp via the step-flow, layer-by-layer growth mechanism.

Figure 3(k-n) illustrate HRTEM snapshots (supporting Movie 7) showing that atomic layers can also nucleate at the tip corner. These atomic layers propagate toward the left side via step-flow growth and meet up with the atomic layers that are originated from the left-hand corner of the tip and propagate in the opposite direction, thereby filling up the trough region in between. One can see that the atomic step indicated by arrow “1” and the atomic step indicated by arrow “2” are propagating towards each other (Figure 3(k)). It should be noted in Figure 3(k) that atomic step “1” is nucleated at the top right-hand corner of the tip as marked by the green triangle while step “2” is nucleated at the left-hand corner that is out of the field of the TEM view. In Figure 3(l), steps 1 and 2 have annihilated by their perfect merging with the two atomic steps propagating toward each other, leading to the growth of a complete new atomic layer over the tip terrace. With the continuous supply of Cu ions to the nanowire tip through the bicrystal grain boundary diffusion, several more atomic layers nucleate preferentially at the top right-hand corner of the tip, which results in a locally higher plateau at the corner, as indicated by the

arrows in Figure 3(l, m). The step-flow growth of these atomic layers toward the left and their subsequent merging with propagating atomic layers from the opposite direction results in the flattening of the tip, as shown in Figure 3(m, n). Similar to that shown in Figure 2, the *in situ* TEM observations shown here demonstrate that the growth of the atomic layers does not sweep across the top-left and top-right corners of the tip toward the side facets. Figure 3(o) schematically illustrates the nucleation and growth process of atomic layers at the nanowire tip, as revealed from the *in situ* TEM observations, that is, atomic layers nucleate in the corner regions of the nanowire tip and the merging of these atomic layers by their layer-by-layer, step-flow growth leads to the nanowire lengthening at the tip.

To further substantiate the bicrystal grain boundary diffusion process leading to the nanowire tip growth as shown above, we perform density-functional theory (DFT) modeling of the diffusion processes of Cu ions. We first evaluate the diffusion barriers of Cu ions along a bicrystal grain boundary. Different types of bicrystal grain boundaries have been experimentally observed in CuO nanowires.^[9a] Modeling a high-index grain boundary like the one shown in Figure 1(c) is computationally challenging because of the large number of atoms needed for building the supercell. Therefore, we choose the low-index and symmetrical (002)/(002) boundary to model the bicrystal boundary diffusion. This boundary has been widely observed in experiments^[9a] and **Figure 4(a)** shows its atomic structure viewed along the direction parallel to the (002) bicrystal plane. Diffusion by direct lattice exchange via adjacent atoms is likely to be inhibited by the large barrier associated this process. Additionally, it is well established that the cation-vacancy exchange mechanism dominates the atomic diffusion processes in the oxide growth during the oxidation of Cu.^[5b, 16] As shown in Figure 4(b), there is only one type of

crystallographically non-equivalent Cu vacant sites in the (002) plane. This leads to three possible paths for the cation-vacancy exchange within the bicrystal plane, as shown by the arrow directions in Figure 4(b). The diffusion barriers for these three paths are calculated to be 1.54 eV, 1.55 eV, and 0.76 eV, respectively. The calculations indicate that there is indeed anisotropic diffusion, where the barrier for the diffusion along the most favorable direction is rather small (0.76 eV), only half of the barriers for the diffusion along the other two directions.

After Cu ions are delivered by the bicrystal grain boundary diffusion to the nanowire tip, they will react with adsorbed oxygen leading to the nanowire lengthening. There are two important kinetic energy parameters involved in a tip growth process, that is, the surface diffusion barrier and corner-crossing barrier. The former controls the surface diffusion of Cu ions on the tip, and the latter controls the transport of Cu ions from the nanowire tip to the sidewall, which resembles a three-dimensional version of the Ehrlich–Schwoebel (ES) barrier.^[4c, 17] The corner-crossing barrier represents the extra energy barrier that hinders the crossing of an adatom over a corner, that is, the transport of Cu ions from a tip facet to the side facet. We perform DFT calculations to evaluate the magnitudes of the surface diffusion barrier and corner-crossing barrier in our system. Our DFT modeling is based on the tip geometry shown in Figure 3(a), in which the nanowire tip is terminated with the $(1\bar{1}1)$ plane along with a side facet of $(\bar{1}1\bar{3})$. Cu ions are first delivered through the bi-crystal boundary diffusion to the $(1\bar{1}1)$ tip, followed by surface diffusion on the $(1\bar{1}1)$ facet and possibly further diffusing to the $(\bar{1}1\bar{3})$ side facet via overcoming the corner-crossing barrier. As shown in Figure 4(c), sites “1”, “2” and “3” are stable sites for Cu ions on the tip terrace and the side facet, respectively. The barrier for the surface diffusion of a Cu ion from site 1 to 2 is 0.8 eV. By contrast, the barrier for a Cu ion

crossing the corner from site “2” to site “3” is 1.62 eV. Therefore, the Cu ion encounters a significantly larger barrier for the corner crossing from the $(1\bar{1}1)$ tip to the $(\bar{1}1\bar{3})$ side facet. The presence of the corner-crossing barrier impedes the diffusion of Cu ions from the tip terrace to the sidewall, and Cu ions are easily bounced back when they approach the tip terrace-sidewall corner, facilitating unidirectional growth of nanowires along the axis direction. This results in the nucleation of new atomic steps in the tip corner region (Figure 2(m-p), Figure 3) or even the middle of the tip terrace (Figure 2(i-l)) due to the small width of the nanowire tip. It can be noted that the barrier (0.8 eV) for surface diffusion is similar to that (0.76 eV) for the bicrystal grain boundary diffusion along the most favorable pathway (shown in Figure 4(b)). This suggests that the bicrystal grain boundary diffusion can be as efficient as the surface diffusion, which explains the overgrowth of new oxide (protrusion) at the bicrystal grain boundary location of the nanowire tip (Figure 2) because of the fast arriving rate of Cu ions delivered by the bicrystal grain boundary diffusion.

The preferential nucleation and growth of new atomic layers on the nanowire tip clearly points to the effect of the corner-crossing barrier in modulating the surface concentration of Cu adatoms and thus the thermodynamic driving force of new oxide formation at the tip. Because the corner-crossing barrier hinders Cu ions crossing descendent steps from the tip terrace to the sidewall of the nanowire, Cu ions bounce back from the intersecting edge of the tip and sidewall. This, therefore, results in a higher concentration of Cu ions across the tip terraces, thereby giving rise to the nucleation of CuO atomic layers in the different regions of the nanowire tip, as observed in Figure 2 and 3. The corner-crossing barriers for hindering the crossover of Cu ions from the tip terrace to the sidewall result in the accumulation of Cu ions across the nanowire tip,

which promote the lengthening while limiting the widening (diameter) of the growing nanowire. However, there are still some Cu ions capable of crossing over the tip corner and reaching the sidewall of the nanowire, thereby resulting in the slow sidewall growth by step-flow propagation of atomic layers on the sidewalls along the direction from the nanowire tip towards the root. **Figure 5(a)** is a low-magnification TEM image displaying a bi-crystal nanowire used to observe the sidewall growth. Sky arrows suggest the kinetic pathways for Cu diffusion, that is, Cu ions are first delivered by the bicrystal grain boundary diffusion to the nanowire tip, followed by surface diffusion for the nanowire growth at the tip and along the sidewall. The electron diffraction pattern in the bottom panel of Figure 5(a) is obtained from the left-hand grain, as marked by the yellow dashed square in Figure 5(a), from which it can be determined that the sidewall is terminated by the (110) facets and the adjacent sidewall vertical to the incident e-beam direction is (001), as shown schematically shown in Figure 5(c).

Figure 5(b) shows time-sequence HRTEM images (extracted from supporting *in situ* TEM Movie 8) captured from a region along the sidewall marked by the green rectangle in Figure 5(a). It can be seen that an atomic step is propagating via the step-flow growth towards the root of the nanowire along the sidewall. Along with the upward growth at the nanowire tip as shown above in Figure 1-3, the downward growth of the atomic layers on the sidewall confirms the bicrystal grain boundary diffusion mechanism that delivers Cu ions to the nanowire tip, followed by the descendent diffusion of Cu ions from the tip to the sidewall. The corner-crossing barrier effect in hindering the tip-sidewall jumps of Cu ions makes the lateral growth much slower than the axial growth. As seen in Figure 5(b), the step-flow growth of the atomic layer on the sidewall occurs via an adatom mechanism, that is, Cu and O ions are added onto the growth

front of the step edge via surface diffusion, where Cu ions are supplied from the nanowire tip via the bicrystal grain boundary diffusion. However, the *in situ* TEM observations illustrate that step-flow growth shows an oscillatory behavior. The sky arrows in Figure 5(b) mark the location of the leading edge of the atomic layer on the (110) sidewall viewed from the TEM edge-on imaging, which is seen to undergo cycles of advancement, stopping, retraction, and regrowth. This non-monotonic oxide growth is further confirmed by the oscillatory motion of the growth front of the atomic layer on the adjacent (001) sidewall, which is in the planar view of the TEM imaging. As seen in Figure 5(b), a step edge indicated by the yellow arrows is present on the planar (001) surface. As the atomic overlayer grows, its leading edge behaves like a moving step, and undergoes the same oscillatory cycles of advancement, stopping, retraction, and regrowth as the one on the (110) sidewall. It is worth noting from Figure 5(b) (and supporting *in situ* TEM Movie 8) that the CuO bulk lattice remains stationary with respect to the advancement/retraction of the leading edge of the atomic overlayers, for which any possible oscillatory specimen drift can be ruled out. The observed oscillatory growth of the atomic layers on the (110) and (100) sidewall facets is schematically illustrated in Figure 5(c).

The advancement and retraction motion of the growth front of the oxide layer is related to the oxide growth and decomposition at the step edge of the oxide layer. Such non-monotonic oxide growth cannot be attributed to any temperature and oxygen pressure effect because their fluctuations are negligible for such fast oscillating cycles (\approx one cycle per second). Instead, the oscillatory growth can be induced by the curvature effect at the growth front. This can be evidenced by measuring the angle formed between the line along the leading edge of the growing oxide layer on the (001) sidewall and the line of the intersection of the (001) and (110) sidewall facets, as indicated in Figure 5(b). As seen from *in situ* TEM video 6 and Figure 5(b), the leading

edge of the oxide layer grows faster along the intersecting line of the (110) and (100) sidewall facets. Therefore, θ decreases from $\approx 42.8^\circ$ to $\approx 37.4^\circ$ as the leading edge of the growth front of the overlayer advances while it increases from $\approx 37.4^\circ$ to $\approx 41.8^\circ$ as the leading edge of the overlayer retracts. Therefore, the advancement/retraction motion of the leading edge of the growth front of the oxide layer depends on the range of the intersection angle θ that is measured via the overlapping-induced shadow (as shown schematically in Figure 5(c)), which in turn controls the coordination number of the atoms at the leading edge of the oxide layer. Our measurements indicate that the leading edge of the oxide layer advances when θ is $> 41^\circ$ while it retracts when θ becomes close to $\approx 37^\circ$ or smaller. This indicates that the Cu and O atoms at the step edge of the growth front can be stabilized with the increased number of coordination atoms for the relatively large θ , thereby promoting the oxide growth. By contrast, there are less coordination atoms at the step edge for the smaller θ , which in turn results in oxide decomposition at the leading edge of the oxide layer.

Figure 6 summarizes schematically the atomic processes underlying the CuO nanowire growth as revealed from the combined *in situ* TEM observations and DFT calculations. The oxidation of Cu in the intermediate temperature range ($\approx 300\text{--}550^\circ\text{C}$) is dominated by grain boundary diffusion.^[6-7] Cu ions are delivered by grain boundary diffusion to the outer surface adjacent to the grain boundary. This leads to locally faster oxide growth of adjacent CuO grains in the grain boundary region, which in turns results in the nucleation and growth of a CuO bicrystal nanowire (Figure 6(a, b)). The locally faster oxide growth at the grain boundary is also evidenced by the observed protruding oxide growth at the nanowire tip shown in Figure 2. The nanowire lengthening occurs by tip growth, where Cu ions are pumped to the nanowire tip via

bicrystal grain boundary diffusion, followed by surface diffusion induced step-flow growth at the tip (Figure 6(c-e)). The bicrystal grain boundary diffusion mechanism is also supported by the observed downward growth of atomic layers on the nanowire sidewall (Figure 5), where Cu ions are delivered through bicrystal grain boundary diffusion from the nanowire root to the tip, followed by subsequent surface diffusion from the tip to the sidewall. By contrast, no upward propagation of atomic layers along the sidewall adjacent to the tip region was observed, indicating that the bottom-up sidewall diffusion is limited to the root region (for the lateral growth) without reaching the nanowire tip. Meanwhile, Cu ions are also delivered onto the CuO substrate surface via outward grain diffusion, most of which are trapped by surface defects of the CuO substrate without diffusing for a long distance because the CuO substrate surface is not atomically flat (as shown in Figure 1), where the high density of surface defects such as atomic steps, kinks, ledges and vacancies results in the surface growth of the CuO substrate. However, there is still a small fraction of Cu ions capable of diffusing to the nanowire sidewall, which results in the lateral growth of the nanowire in the root region (Figure 6(c-e)). This is also evidenced by the in-situ TEM observations showing the slow increase in the nanowire diameter near the base region (Figure 1). Similarly, the high density of surface defects in the nanowire root region (as shown schematically in the inset of Figure 6(e)) impedes the long-distance diffusion of Cu ions along the nanowire sidewall, for which Cu ions are trapped in the root region and react with surrounding oxygen to form new oxide. Therefore, the nanowire root is gradually buried with the CuO growth at the substrate surface, as shown in Figure 1(a). This is in contrast to the nanowire lengthening at the tip, where the synergetic effect of the small energy barrier of the bicrystal grain boundary diffusion (Figure 4) for delivering Cu ions from the root to the tip and the large corner-crossing barrier in hindering the crossover of Cu ions from the

nanowire tip to the sidewall (Figure 4) greatly promotes the unidirectional oxide growth. This suggests that Cu ions delivered by the bicrystal grain boundary diffusion are largely incorporated into the nanowire tip. This is also consistent with the in-situ TEM observations (Figure 5) showing that the downward propagation of the atomic layers on the sidewall is highly oscillatory with a much slower overall rate than the step-flow growth at the nanowire tip (Figure 2-3) because of the lack of sufficient Cu ions from the nanowire tip. Therefore, the diameter of the nanowires is controlled by the step flow growth at the nanowire tip. The nanowire thickening via the downward growth of atomic layers on the nanowire sidewall is largely suppressed because the large corner-crossing barrier restrains the transfer of Cu ions from the nanowire tip to the sidewall. Meanwhile, the nanowire root region experiences some lateral growth via upward surface diffusion (at short distances) of Cu ions along the nanowire sidewall. As a result, the nanowires typically are tapered with a larger diameter at the root (Figure 1).

The favored grain boundary diffusion over the surface diffusion for the delivery of Cu ions to the nanowire tip is also related to the existence of a large number of Cu vacancies in the Cu oxides. It has been well established in the literature that the Cu oxides (Cu_2O and CuO) formed from the oxidation of Cu is intrinsically Cu deficient with large deviations from the stoichiometry.^[6, 18] Our DFT computations show the tendency for Cu vacancies to segregate to the bicrystal grain boundary (Figure S3). This therefore results in a higher concentration of Cu vacancies at the grain boundary and thus promotes the grain boundary diffusion (via the atom-vacancy exchanges) of Cu ions to the nanowire tip.

Our TEM observations show that bicrystal grain boundaries are present in nearly all the CuO nanowires formed from the oxidation of Cu (Figure S4). This is also consistent with a large body of previous studies showing the presence of bicrystal grain boundaries in oxide nanowires

from the oxidation of metals.^[1a, 1e, 9a, 10] The complementary information from our TEM and SEM observations and DFT modeling is mutually consistent and delivers strong evidence for the grain-boundary diffusion controlled anisotropic oxide growth. However, it is also noted that there were a few reports showing the formation of single-crystal CuO nanowires.^[19] In this case, the absence of grain boundaries in the nanowires can make the bottom-up surface diffusion along the nanowire sidewall as the dominant mechanism for the nanowire growth.

The growth of oxide nanostructures with various morphologies such as nanowires, nanoblades, nanobelts, or nanoplatelets has been extensively observed from the oxidation of metals and alloys including Cu^[3b, 20], Fe^[21], Ni^[22], Zn^[23], Mo^[24], and Cu-Zn^[25]. A common microstructure feature observed in these oxide nanostructures is the presence of bicrystal grain boundaries, but little has been known so far about whether the grain boundaries play any important role in controlling the mass transport process in the oxide growth and leading to the different growth morphologies. Based on the TEM observations presented above, we see that the bicrystal grain boundaries serve as the short circuit paths for the transport of metal ions from the root region to the nanowire tip for unidirectional crystal growth. Since the growth of these oxide nanostructures relies closely on the grain boundary diffusion. It is reasonable to expect that any control over the grain boundary structure can lead to the control over the oxide growth. As illustrated schematically in Figure 6, a higher density of grain boundaries in the underlying CuO layer can result in more surface sites for nucleating CuO nanowires. Indeed, it has been shown that the microstructure feature of the metal substrate, especially the grain size and surface roughness, can significantly influence the formation and growth of oxide nanowires.^[1d, 19a, 26] For instance, sandblasting can be employed to increase the surface roughness of the metal substrate that results in finer grains in the layered oxide growth, thereby promoting oxide nanowire

formation and exerting control over the oxide growth morphologies (nanowires vs nanolades).^[5b, 21a, 21b] The difference in the growth morphologies, that is, 1D nanowires^[3b, 5b, 27] vs. 2D nanobelts/nanobelts/nanoplatelets^[21a, 21b, 21d], can be attributed to the effect of the atomic structure at the bicrystal grain boundary. For the nanowire growth, the bicrystal grain boundary has an anisotropic structure, for which the diffusion along the bicrystal plane can be highly anisotropic. By contrast, an isotropic bicrystal grain boundary structure promotes the more isotropic diffusion along the bicrystal plane, which results in platelet growth with the wide and thin geometry.

3. Conclusion

In summary, we have provided evidence for the correlation between the nanowire growth and bicrystal grain boundary diffusion. Our *in situ* HRTEM observations demonstrate that the bicrystal grain boundary is the preferred diffusion pathway for the transport of metal species from the nanowire root to the tip for the nucleation and step-flow growth of atomic planes at the tip. The observed step-flow propagation of atomic layers from the nanowire tip toward the root direction further confirms the bicrystal grain boundary diffusion mechanism for the nanowire growth. We show that the corner-crossing barriers play an important role in promoting the unidirectional oxide growth at the nanowire tip by hindering the transport of Cu ions from the nanowire tip to the sidewall facets. The broadly observed bicrystal boundaries in various oxidation-induced oxide nanostructures indicate the universal character of the bicrystal grain boundary diffusion mechanism and point to its unique role in tuning the growth morphology by controlling the bicrystal grain boundary structure that promotes one-dimensional crystal growth

with the anisotropic bicrystal grain boundary diffusion or two-dimensional growth with more isotropic diffusion along the bicrystal grain boundary plane.

4. Experimental Section

CuO nanowire formation was examined by both *ex situ* and *in situ* experiments. For *ex situ* experiments, high-purity copper foils (99.999 % purity) were first thoroughly rinsed with deionized water followed by ultrasonication in acetone for 5 min. After drying, the cleaned copper foils were placed on a substrate heater in the vacuum chamber and the sample temperature was monitored using a K-type thermocouple in contact with the sample heater. The chamber was pumped to vacuum ($\approx 2.67 \times 10^{-4}$ Pa), and then filled with 2.67×10^4 Pa oxygen pressure (99.999% oxygen). The chamber was then sealed, and the Cu sample was heated to the desired temperature (400 °C) at 20 °C min^{-1} in the oxygen gas. After the Cu sample was oxidized for 2h, it was cooled down in the same oxygen atmosphere to room temperature at the rate of $\approx 10 \text{ °C min}^{-1}$. Growth morphology and chemical composition of the oxidized samples were examined using a field emission scanning electron microscopy. For *in situ* experiments, the cleaned high-purity foil was loaded onto a furnace-based TEM heating holder that was plasma cleaned. The heating holder was then loaded in a dedicated ETEM column, equipped with a post-specimen image corrector and a gas manifold that enables flowing different gases at controlled flow rate to obtain desired partial pressure in the sample area. In our experiments, pure oxygen (99.9999 % purity) was introduced into the sample area in the ETEM column at a partial pressure of ≈ 0.5 Pa. The sample was then heated up to 400 °C in the flow of the oxygen gas. *In situ* observation of the CuO nanowire growth was conducted at 300 kV. In all the experiments,

unless otherwise mentioned, the dose rate for recording TEM images was controlled in the range of $3.4 \sim 8.3 \times 10^4$ e/(nm²s). The growth process was monitored by low magnification and high-resolution TEM (HRTEM) images and videos, and nano-beam electron diffraction. *In situ* HRTEM imaging of the oxide nanowire growth was performed at a frame rate of 0.1 s⁻¹.

Spin-polarized DFT calculations were performed using the Vienna Ab-initio Simulation Package (VASP) with a plane-wave basis set.^[28] PBE generalized gradient approximation (GGA) was used to describe the electron–electron exchange and correlation interactions. The Brillouin zones of the CuO bulk and surface slab were sampled using the $(8 \times 8 \times 8)$ and $(4 \times 2 \times 1)$ Monkhorst-Pack meshes, respectively.^[28c] Considering the strong correlation effect among the partially filled Cu 3d states in CuO, we have employed the DFT+U method with $U = 7$ eV and $J = 0$ eV.^[29] As a result, we obtained an antiferromagnetic ground state, with a local magnetic moment close to 0.67 μ B for 4-fold coordinated Cu²⁺ cations in the simulated CuO, which is in good agreement with the experimental values.^[30] The optimized structural parameters using the bulk CuO model are $a=0.449$ nm $b=0.367$ nm, $c=0.512$ nm, $\beta=96.1^\circ$, respectively. The surfaces were modeled using a periodically repeated slab consisting of alternate 6-lattice spacing $(1\bar{1}1)$ terraces separated by 4-atomic wide (002) facets. Successive slabs with 8 atomic layers are separated with a vacuum region of 1.2 nm. The atoms in the bottom two layers of the slab were fixed while the other layers of the slab were allowed to relax until the force components acting on each of the atoms are less than 0.15 eV/nm.

Supporting Information

Supporting Information is available from the Wiley Online Library or from the author.

Acknowledgements

X. H. Sun and W. H. Zhu contributed equally to this work. The authors would like to thank Prof. Judith C Yang at the University of Pittsburgh for the help with this work. This work was supported by the U.S. Department of Energy, Office of Basic Energy Sciences, Division of Materials Sciences and Engineering under Award No. DE-SC0001135. This research used resources of the Center for Functional Nanomaterials, which is a U.S. DOE Office of Science Facility, and the Scientific Data and Computing Center, a component of the Computational Science Initiative, at Brookhaven National Laboratory under Contract No. DE-SC0012704. This work also used the computational resources from the Extreme Science and Engineering Discovery Environment (XSEDE) through allocation TG-DMR110009, which is supported by National Science Foundation grant number OCI-1053575.

Disclaimer: Certain commercial equipment, instruments, or materials are identified in this paper in order to specify the experimental procedure adequately. Such identification is not intended to imply recommendation or endorsement by the National Institute of Standards and Technology, nor is it intended to imply that the materials or equipment identified are necessarily the best available for the purpose.

Conflict of Interest

The authors declare no conflict of interest.

Received: ((will be filled in by the editorial staff))

Revised: ((will be filled in by the editorial staff))

Published online: ((will be filled in by the editorial staff))

References

- [1] a) X. C. Jiang, T. Herricks, Y. N. Xia, *Nano Lett.* **2002**, 2, 1333; b) A. Kolmakov, M. Moskovits, *Annu. Rev. Mater. Res.* **2004**, 34, 151; c) E. Comini, C. Baratto, G. Faglia, M. Ferroni, A. Vomiero, G. Sberveglieri, *Prog. Mater. Sci.* **2009**, 54, 1; d) G. Filipič, U. Cvelbar, *Nanotechnology* **2012**, 23, 194001; e) Q. B. Zhang, K. I. Zhang, D. G. Xu, G. C. Yang, H. Huang, F. Nie, C. M. Liu, S. H. Yang, *Prog. Mater. Sci.* **2014**, 60, 208.
- [2] a) K. G. Compton, A. Mendizza, S. M. Arnold, *Corrosion* **1951**, 7, 327; b) R. Takagi, *J. Phys. Soc. Jpn.* **1954**, 9, 162; c) R. TAKAGI, *Microscopy* **1955**, 3, 18; d) S. M. Arnold, S. E. Koonce, *J. Appl. Phys.* **1956**, 27, 964; e) R. Takagi, *J. Phys. Soc. Jpn.* **1957**, 12, 1212.
- [3] a) G. Filipič, O. Baranov, M. Mozetič, U. Cvelbar, *J. Appl. Phys.* **2015**, 117, 043304; b) L. Yuan, Y. Q. Wang, R. Mema, G. W. Zhou, *Acta Mater.* **2011**, 59, 2491.
- [4] a) R. Sharma, *Microsc. Microanal.* **2001**, 7, 494; b) G. W. Zhou, L. L. Luo, L. Li, J. Ciston, E. A. Stach, J. C. Yang, *Phys. Rev. Lett.* **2012**, 109, 235502; c) L. Li, L. L. Luo, J. Ciston, W. A. Saidi, E. A. Stach, J. C. Yang, G. W. Zhou, *Phys. Rev. Lett.* **2014**, 113, 136104; d) L. F. Zou, J. Li, D. Zakharov, E. A. Stach, G. W. Zhou, *Nat. Commun.* **2017**, 8, 307; e) L. F. Zou, C. M. Yang, Y. K. Lei, D. Zakharov, J. M. Wiezorek, D. Su, Q. Y. Yin, J. Li, Z. Y. Liu, E. A. Stach, J. C. Yang, L. Qi, G. F. Wang, G. W. Zhou, *Nat. Mater.* **2018**, 17, 56.
- [5] a) R. Mema, L. Yuan, Q. T. Du, Y. Q. Wang, G. W. Zhou, *Chem. Phys. Lett.* **2011**, 512, 87; b) L. Yuan, G. W. Zhou, *J. Electrochem. Soc.* **2012**, 159, C205.
- [6] N. Birks, G. H. Meier, F. S. Pettit, *Introduction to the high temperature oxidation of metals*, Cambridge University Press, **2006**.
- [7] Y. f. Zhu, K. J. Mimura, M. Isshiki, *Mater. Trans.* **2002**, 43, 2173.
- [8] a) E. I. Givargizov, **1975**, 20; b) Y. Kong, D. Yu, B. Zhang, W. Fang, S. Feng, *Appl. Phys. Lett.* **2001**, 78, 407; c) T. Yanagida, K. Nagashima, H. Tanaka, T. Kawai, *Appl. Phys. Lett.* **2007**, 91, 061502; d) G. W. Zhou, J. C. Yang, F. Xu, J. A. Barnard, Z. Zhang, *Mater. Res. Soc. Symp. Proc.* **2003**, 737, F6.3.1.
- [9] a) H. P. Sheng, H. Zheng, S. F. Jia, L. Li, F. Cao, S. J. Wu, W. Han, H. H. Liu, D. S. Zhao, J. B. Wang, *J. Appl. Crystallogr.* **2016**, 49, 462; b) L. Yuan, Q. Y. Yin, Y. Q. Wang, G. W. Zhou, *Chem. Phys. Lett.* **2013**, 590, 92.
- [10] S. Rackauskas, H. Jiang, J. B. Wagner, S. D. Shandakov, T. W. Hansen, E. I. Kauppinen, A. G. Nasibulin, *Nano Lett.* **2014**, 14, 5810.
- [11] A. G. Nasibulin, S. Rackauskas, H. Jiang, Y. Tian, P. R. Mudimela, S. D. Shandakov, L. I. Nasibulina, S. Jani, E. I. Kauppinen, *Nano Res.* **2009**, 2, 373.
- [12] a) F. M. Ross, *Rep. Prog. Phys.* **2010**, 73, 114501; b) F. Panciera, Y. C. Chou, M. C. Reuter, D. Zakharov, E. A. Stach, S. Hofmann, F. M. Ross, *Nat. Mater.* **2015**, 14, 820.
- [13] H. Amekura, O. A. Plaksin, K. Kono, Y. Takeda, N. Kishimoto, *J. Phys. D: Appl. Phys.* **2006**, 39, 3659.
- [14] a) B. J. Hansen, G. H. Lu, J. H. Chen, *J. Nanomater.* **2008**, 2008, 48; b) C. H. Xu, C. H. Woo, S. Q. Shi, *Superlattices Microstruct.* **2004**, 36, 31.

- [15] C. Wagner, *Z. Phys. Chem.* **1933**, 21, 25.
- [16] a) W. J. Moore, B. Selikson, *J. Chem. Phys.* **1951**, 19, 1539; b) J. A. Van Orman, K. L. Crispin, *Rev. Mineral. Geochem.* **2010**, 72, 757.
- [17] a) G. Ehrlich, F. G. Hudda, *J. Chem. Phys.* **1966**, 44, 1039; b) R. L. Schwoebel, E. J. Shipsey, *J. Appl. Phys.* **1966**, 37, 3682; c) Q. Zhu, W. A. Saidi, J. C. Yang, *J. Phys. Chem. C* **2017**, 121, 11251.
- [18] a) D. J. Young, *High temperature oxidation and corrosion of metals*, Elsevier, **2008**; b) C. Carel, M. Mouallem-Bahout, J. Gaude, *Solid State Ionics* **1999**, 117, 47; c) G. Ettoreche, C. Carel, C. Peslerbe, *Bull. Soc. Sci. Bretagne* **1994**, 65, 71; d) K. R. Lawless, *Rep. Prog. Phys.* **1974**, 37, 231.
- [19] a) A. Kumar, A. K. Srivastava, P. Tiwari, R. V. Nandedkar, *J. Phys.: Condens. Matter* **2004**, 16, 8531; b) L. Liao, Z. Zhang, B. Yan, Z. Zheng, Q. L. Bao, T. Wu, C. M. Li, Z. X. Shen, J. X. Zhang, H. Gong, *Nanotechnology* **2009**, 20, 085203; c) C. Díaz-Guerra, M. Vila, J. Piqueras, *Appl. Phys. Lett.* **2010**, 96, 193105.
- [20] G. Zou, H. Li, D. Zhang, K. Xiong, C. Dong, Y. Qian, *J. Phys. Chem. B* **2006**, 110, 1632.
- [21] a) L. Yuan, Q. K. Jiang, J. B. Wang, G. W. Zhou, *J. Mater. Res.* **2012**, 27, 1014; b) L. Yuan, R. S. Cai, J. I. Jang, W. H. Zhu, C. Wang, Y. Q. Wang, G. W. Zhou, *Nanoscale* **2013**, 5, 7581; c) Y. Q. Wang, C. Wang, L. Yuan, R. S. Cai, X. H. Liu, C. Y. Li, G. W. Zhou, *J. Phys. Chem. C* **2014**, 118, 5796; d) W. H. Zhu, J. P. Winterstein, W. D. Yang, L. Yuan, R. Sharma, G. W. Zhou, *ACS Nano* **2017**, 11, 656.
- [22] a) L. Dufour, F. Morin, *Oxid. Met.* **1993**, 39, 137; b) J. Wang, L. M. Wei, L. Y. Zhang, C. H. Jiang, E. S. W. Kong, Y. F. Zhang, *J. Mater. Chem.* **2012**, 22, 8327.
- [23] a) Y. C. Kong, D. P. Yu, B. Zhang, W. Fang, S. Q. Feng, *Appl. Phys. Lett.* **2001**, 78, 407; b) Y. J. Xing, Z. H. Xi, Z. Q. Xue, X. D. Zhang, J. H. Song, R. M. Wang, J. Xu, Y. Song, S. L. Zhang, D. P. Yu, *Appl. Phys. Lett.* **2003**, 83, 1689; c) L. Yuan, C. Wang, R. S. Cai, Y. Q. Wang, G. W. Zhou, *J. Cryst. Growth* **2014**, 390, 101.
- [24] a) J. Zhou, N. S. Xu, S. Z. Deng, J. Chen, J. C. She, Z. L. Wang, *Adv. Mater.* **2003**, 15, 1835; b) L. Zheng, Y. Xu, D. Jin, Y. Xie, *Chem. Mater.* **2009**, 21, 5681.
- [25] L. Yuan, C. Wang, R. S. Cai, Y. Q. Wang, G. W. Zhou, *J. Appl. Phys.* **2013**, 114, 023512.
- [26] G. Fritz-Popovski, F. Sosada-Ludwikowska, A. Köck, J. Keckes, G. A. Maier, *Sci. Rep.* **2019**, 9, 807.
- [27] L. Yuan, Y. Q. Wang, R. S. Cai, Q. K. Jiang, J. B. Wang, B. Q. Li, A. Sharma, G. W. Zhou, *Mater. Sci. Eng. B* **2012**, 177, 327.
- [28] a) G. Kresse, J. Hafner, *Phys. Rev. B* **1993**, 47, 558; b) G. Kresse, J. Furthmüller, *Phys. Rev. B* **1996**, 54, 11169; c) J. P. Perdew, J. A. Chevary, S. H. Vosko, K. A. Jackson, M. R. Pederson, D. J. Singh, C. Fiolhais, *Phys. Rev. B* **1992**, 46, 6671.
- [29] a) S. L. Dudarev, G. A. Botton, S. Y. Savrasov, C. J. Humphreys, A. P. Sutton, *Phys. Rev. B* **1998**, 57, 1505; b) M. Nolan, S. D. Elliott, *Phys. Chem. Chem. Phys.* **2006**, 8, 5350.
- [30] D. X. Wu, Q. M. Zhang, M. Tao, *Phys. Rev. B* **2006**, 73, 235206.

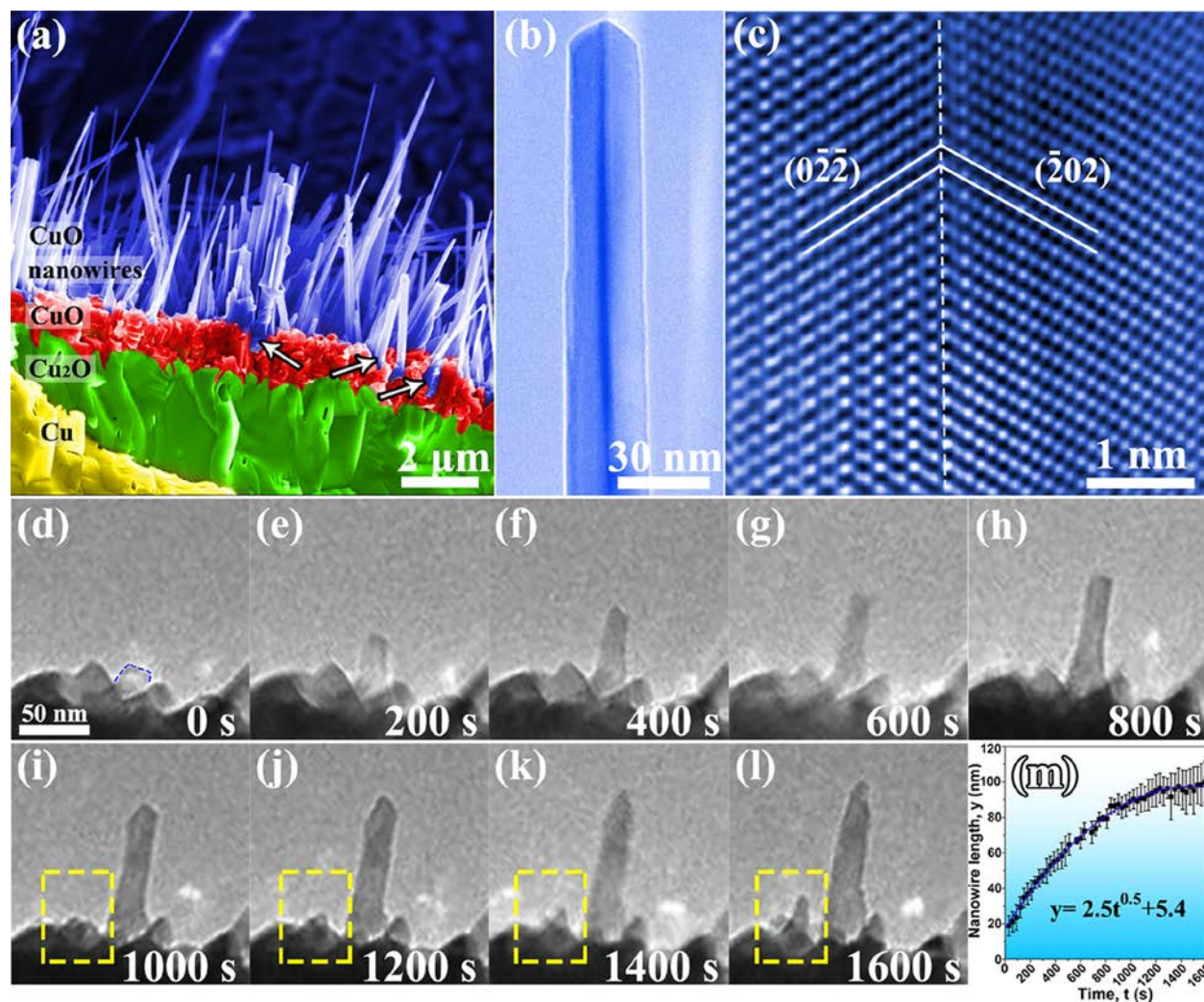


Figure 1. (a) Cross-sectional SEM image of a Cu substrate oxidized at 400 °C and $p_{\text{O}_2} \approx 2.67 \times 10^4$ Pa for 2 h. The white arrows mark the nanowire roots that are buried by the surface growth of the CuO layer. (b) TEM image of a typical CuO nanowire showing a bicrystal grain boundary along the axial direction of the nanowire. (c) HRTEM image showing the presence of an internal bicrystal grain boundary. (d-l) Time-sequenced TEM images (supporting Movie 1) showing the growth of a CuO nanowire during the oxidation of Cu at $T=400$ °C and $p_{\text{O}_2} \approx 0.5$ Pa. The yellow dashed rectangles in (i-l) mark the nucleation and growth of a second CuO nanowire. (m) Time dependence of the growth length of the CuO nanowire measured from *in situ* TEM Movie 1, where the nanowire length is plotted vs. growth time. The

error bars represent standard deviation uncertainties based on multiple measurements. The solid line shows the parabolic fit.

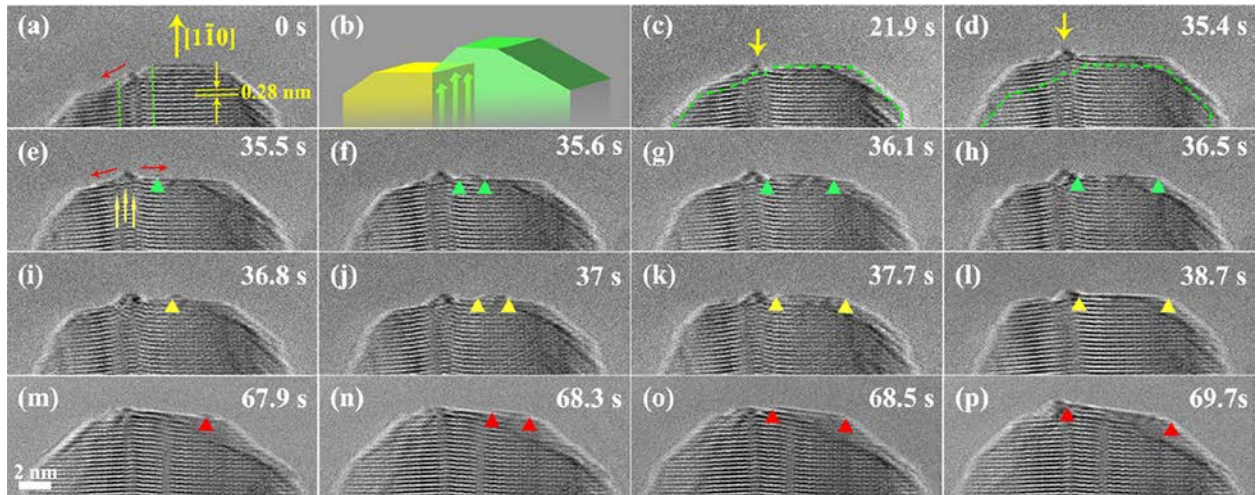


Figure 2. *In situ* TEM observation (supporting Movie 4) of the tip growth of a bi-crystal CuO nanowire during the oxidation of Cu at 400 °C and ≈ 0.5 Pa of O_2 gas flow. (a) A step-terrace configuration at the nanowire tip with a bicrystal grain boundary along the axial direction, the dashed lines mark the projected width of the bicrystal plane. (b) Schematic illustration of the bicrystal grain boundary diffusion for transport of Cu ions from the nanowire root to the tip. (c, d) Nucleation and step-flow growth of new atomic planes on the lower terrace starting from the step-terrace corner of the bicrystal grain boundary location, the dashed green lines in (c) and (d) mark the initial step-terrace configuration seen in (a), the yellow arrows mark the locally faster oxide growth (as a protrusion) at the bicrystal grain boundary. (e-h) nucleation and growth of a new CuO layer on the terrace, the green triangles mark the nucleation location and subsequent step-flow growth of the atomic layer. (i-l) Another sequence of the terrace nucleation and growth of a $(1\bar{1}0)$ layer, the yellow triangles mark the nucleation location and subsequent step-flow growth the atomic layer. (m-p) nucleation and growth of a new CuO layer starting from the top right-hand corner of the tip, the red triangles mark the nucleation location and step-flow growth of the atomic layer.

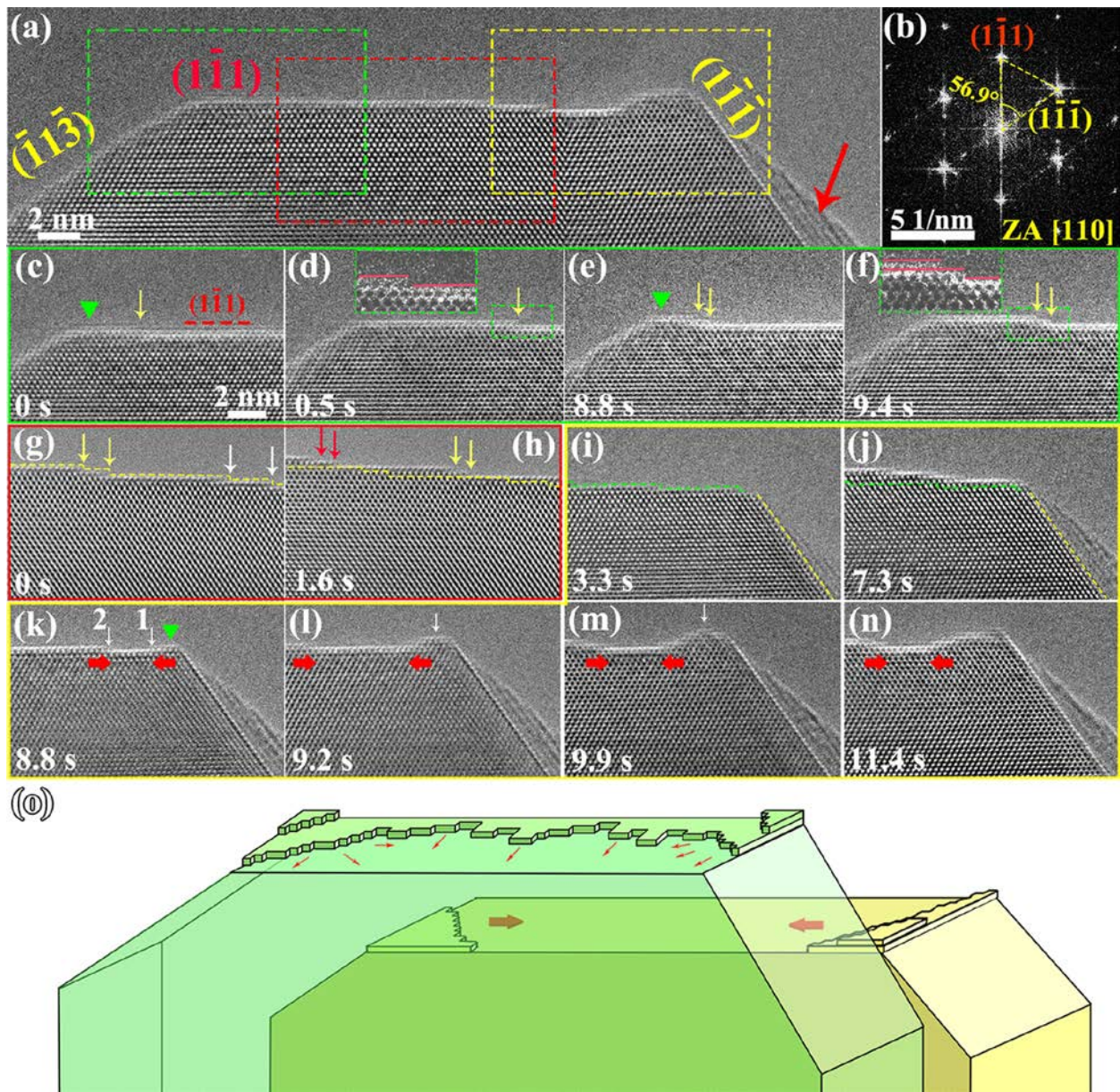


Figure 3. *In situ* TEM imaging of the unidirectional growth of a bi-crystal nanowire at the atomic scale with the viewing direction normal to the bicrystal grain boundary plane during the oxidation of Cu at 400 °C and in ≈ 0.5 Pa of O_2 flow. (a) HRTEM image of the tip region of a CuO tip region, the green, red and yellow dashed rectangles mark the regions chosen for *in situ* TEM visualization of the oxide nucleation and growth. (b) Diffractionogram (fast Fourier transform) of the HRTEM image in (a). (c-f) Time

sequence of HRTEM images (supporting Movie 5) showing the nucleation of monoatomic layers (marked with the green triangles) at the top-left corner of the tip, insets in (d, f) show the zoom-in, contrast-enhanced view of the green dashed box regions. (g, h) Sequential HRTEM images (supporting *in situ* TEM Movie 6) showing the layer-over-layer, step-flow growth of atomic planes on the tip in the middle region. (i-n) Sequential HRTEM images (supporting *in situ* TEM Movie 7) showing the nucleation of atomic layers in the top-right corner region of the nanowire tip and their lateral propagation via the step-flow growth toward the left side. (o) Schematic illustrations of the nucleation and growth process of atomic layers at the nanowire tip with the supply of Cu adatoms to the tip by the bicrystal grain boundary diffusion. Yellow and green colors represent two crystals that form a bicrystal nanowire, with a bicrystal grain boundary in between.

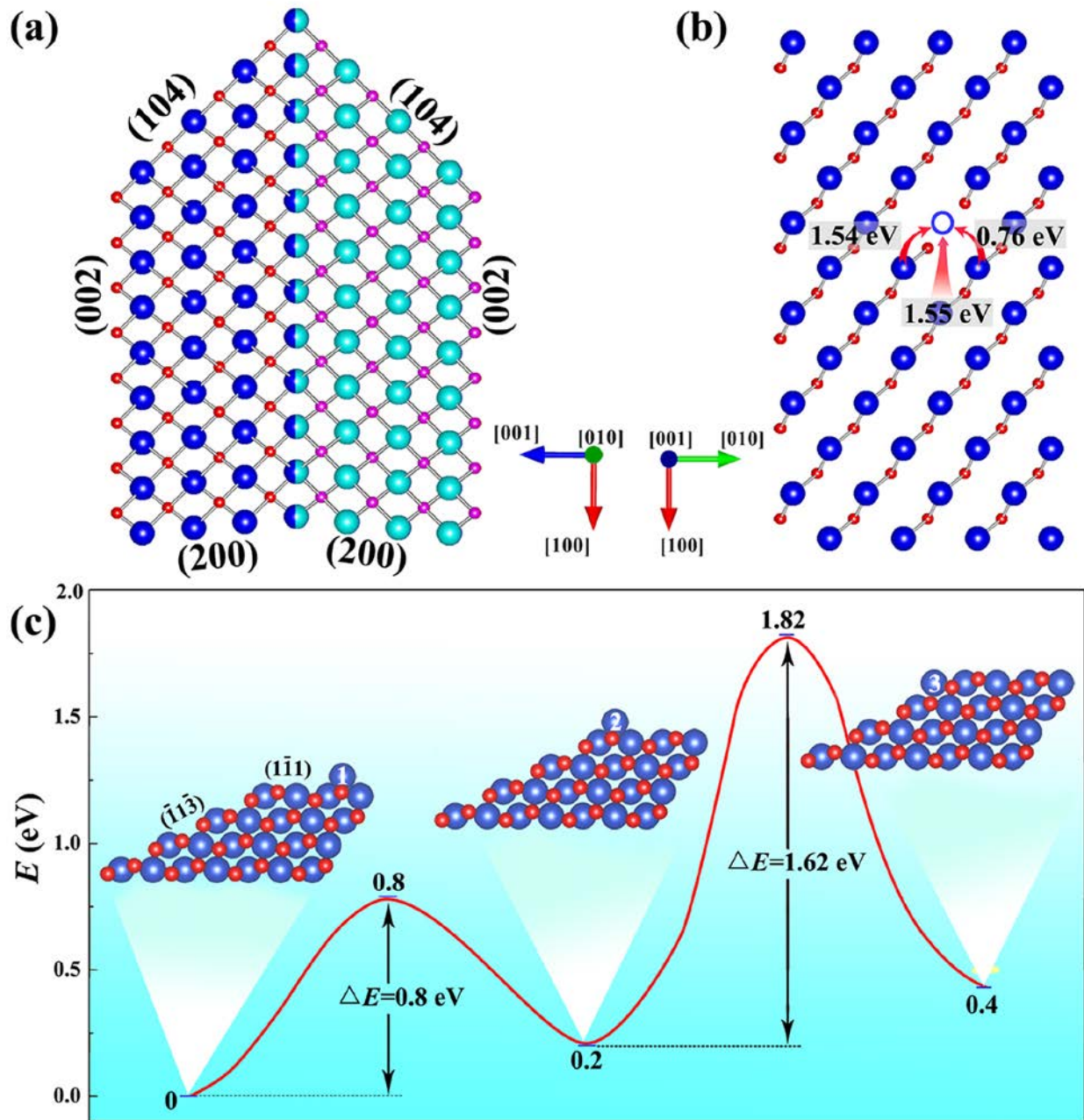


Figure 4. DFT modeling of the cation-vacancy diffusion in the (002)/(002) bicrystal plane. (a) Bicrystal grain boundary structure viewed along the direction parallel to the (002) bicrystal plane. (b) Projection view of the (002) bicrystal grain boundary plane, from which three crystallographically nonequivalent diffusion pathways for cation-vacancy exchanges on the grain boundary plane are identified. (c) DFT

computed minimum energy path for the diffusion of a Cu adatom on the CuO $(\bar{1}\bar{1}1)$ terrace from site 1 to 2 and then to site 3 on the $(\bar{1}1\bar{3})$ side facet. Blue, sky, red, and pink balls represent Cu and O atoms, respectively. The blue open circle in (b) represents a Cu vacancy.

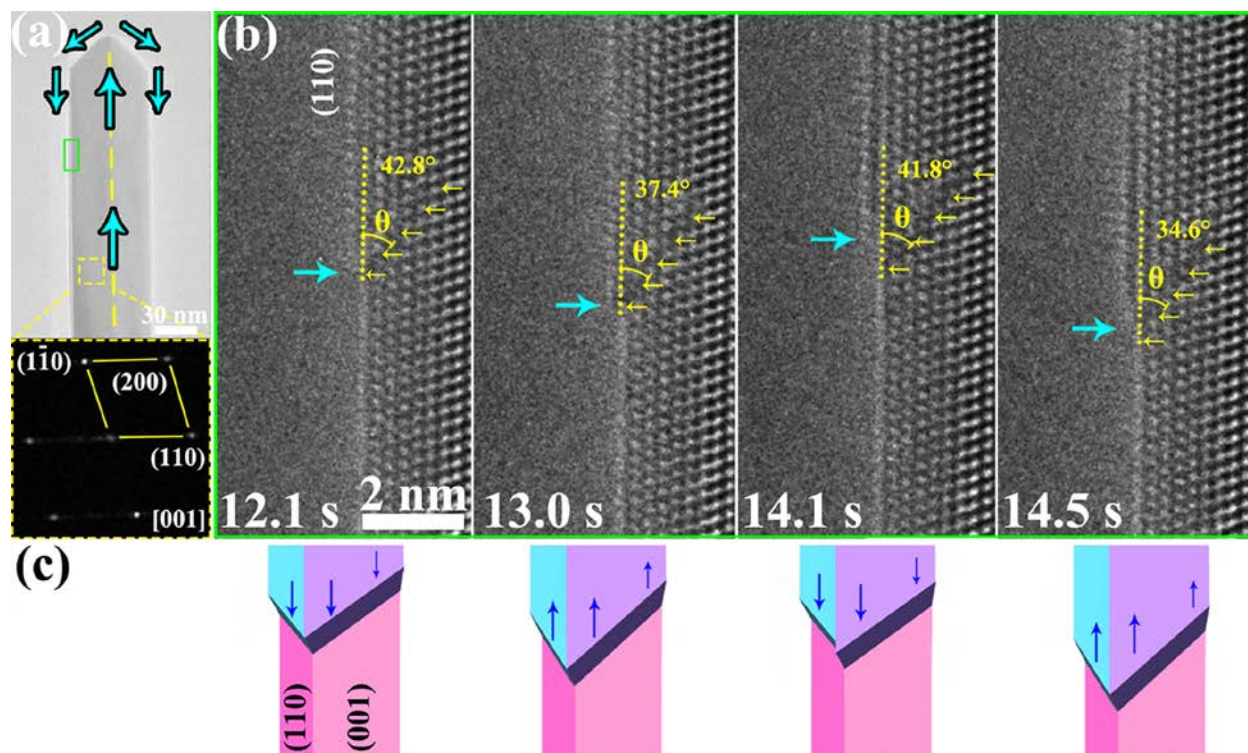


Figure 5. *In situ* HRTEM observation of the oscillatory step-flow growth of a monolayer CuO along the nanowire side facets toward the nanowire root direction during the oxidation of Cu at 400 °C and ≈ 0.5 Pa of O₂ flow. (a) TEM image of a growing CuO nanowire (upper panel) and electron diffraction pattern (bottom panel) from the region marked by the dashed yellow box. The red arrows denote upward diffusion of Cu ions toward the nanowire tip along the bicrystal grain boundary, followed by surface diffusion at the nanowire tip and to the sidewall by crossing over the tip/sidewall corner. (b) Time-sequence HRTEM images (supporting Movie 8) captured from the region marked by the green rectangle in (a), showing the oscillatory propagation of individual atomic layers on the (110) and (001) facets of the adjacent sidewalls. The growth front of the atomic layers is marked with the light blue arrows. (c) Schematic showing oscillatory growth of the oxide overlays along the nanowire sidewall facets.

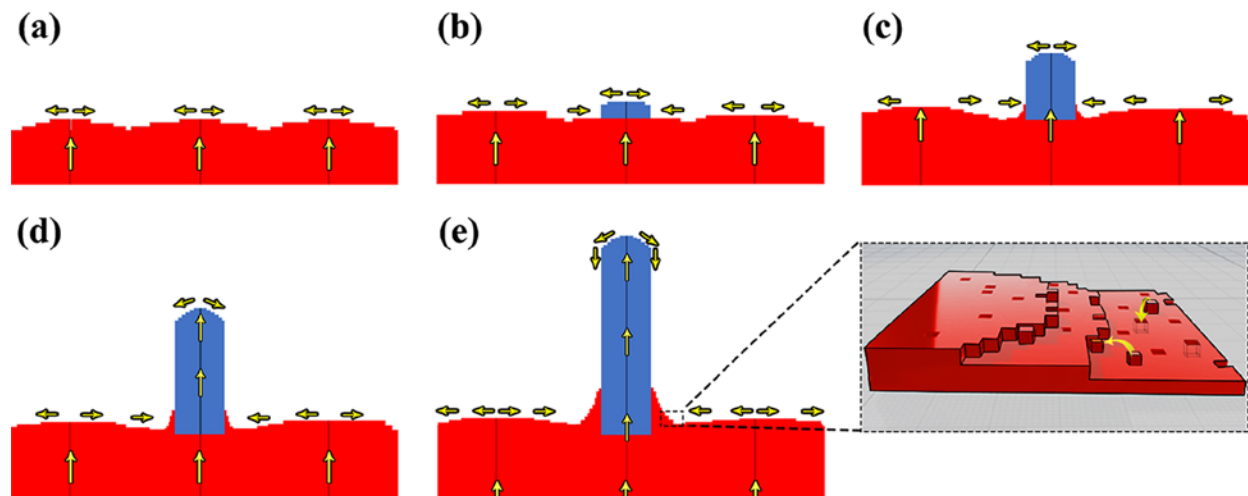


Figure 6. Schematic illustrating the CuO nanowire growth involving both bicrystal grain boundary diffusion and surface diffusion (supporting Movie 9). (a) Oxide growth via outward diffusion of Cu ions through grain boundaries. (b) Sprout-like formation of a bicrystal nanowire from the locally faster oxide growth by the grain boundary diffusion. (c-e) Nanowire tip growth through bicrystal grain boundary diffusion of Cu ions from the root to the tip, followed by step-flow growth at the tip. The nanowire root region undergoes slow lateral growth resulting from the reaction between Cu ions and adsorbed oxygen. Inset: the typical surface morphology of the nanowire root region consisting of a high density of surface defects (steps, kinks, ledges and atomic vacancies) that facilitates oxide growth from the reaction of Cu ions supplied by the bottom-up surface diffusion with readily available oxygen from the surrounding.

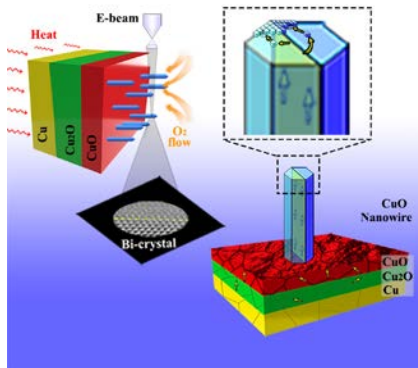
ToC figure text:

Using transmission electron microscopy that spatially and temporally resolves CuO nanowire growth during the oxidation of copper, here we provide direct evidence that bicrystal boundary diffusion is the mass transport mechanism by which Cu ions are delivered from the nanowire root to the tip.

Keyword (Oxide Nanowires)

*Xianhu Sun, Wenhui Zhu, Dongxiang Wu, Zhenyu Liu, Xiaobo Chen, Lu Yuan, Guofeng Wang, Renu Sharma, Guangwen Zhou**

Title (Atomic-Scale Mechanism of Unidirectional Oxide Growth)



ToC figure.

Supporting Information

Atomic-Scale Mechanism of Unidirectional Oxide Growth

Xianhu Sun, Wenhui Zhu, Dongxiang Wu, Zhenyu Liu, Xiaobo Chen, Lu Yuan, Guofeng Wang,

*Renu Sharma, Guangwen Zhou**

This file includes:

Supplemental Figure S1-4

Captions for Supplemental Videos 1-9

Other Supplementary Materials for this manuscript include the following:

Supplemental Videos

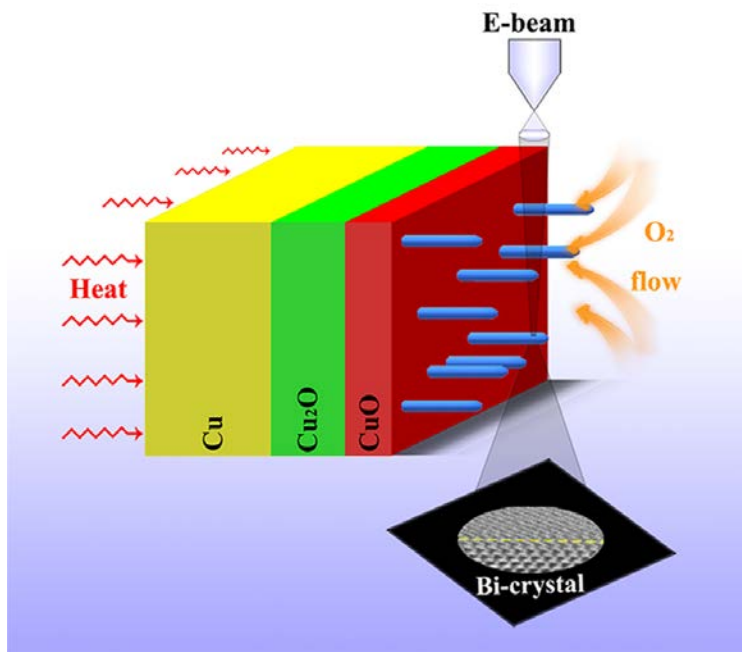


Figure S1. Schematics of the experimental setup for *in situ* TEM observations of the growth of CuO nanowires during the thermal oxidation of Cu.

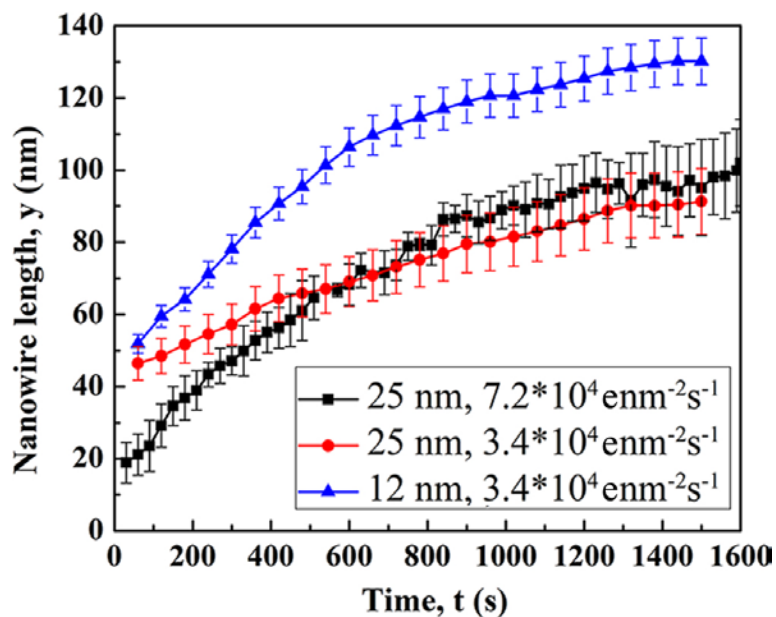


Figure S2. Time dependence of the growth length of the CuO nanowires at $T=400\text{ }^{\circ}\text{C}$ and $p\text{O}_2 \approx 0.5\text{ Pa}$, measured from *in situ* TEM Movies 1-3 captured with the electron dose rates of $3.4 \times 10^4\text{ e}/(\text{nm}^2\text{s})$ and $7.2 \times 10^4\text{ e}/(\text{nm}^2\text{s})$, respectively. The error bars represent standard deviation uncertainties based on multiple measurements. The solid line shows the parabolic fit. It can also be noted that the nanowire with a smaller diameter shows faster length growth.

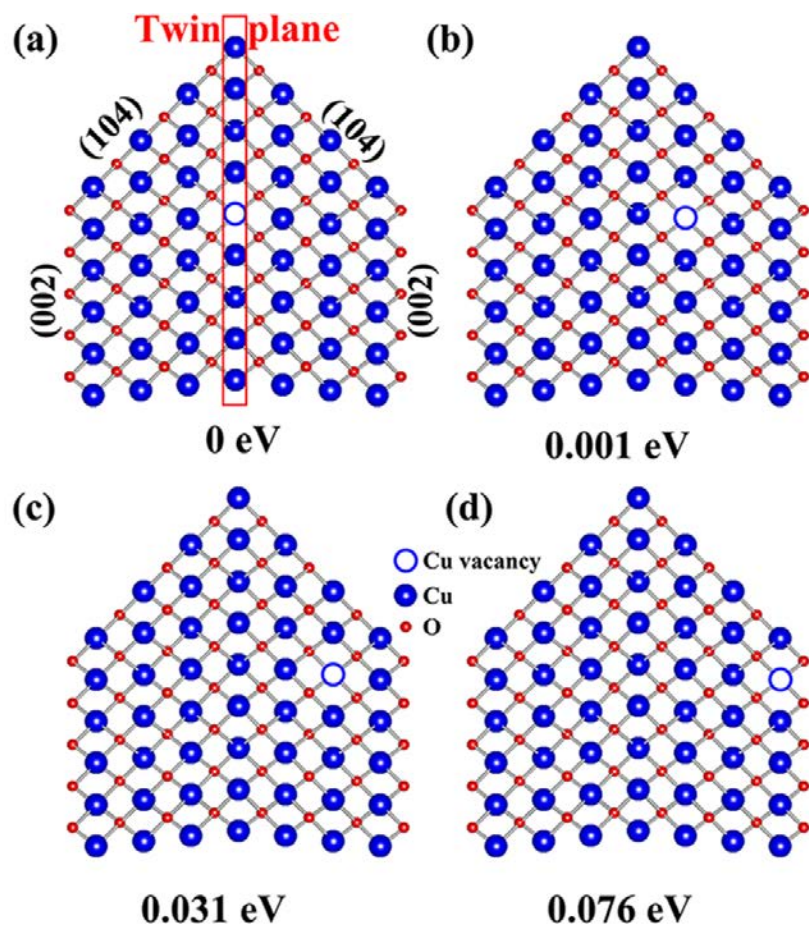


Figure S3. DFT calculations of the grain boundary segregation of a Cu vacancy (blue circle). (a) The Cu vacancy at the grain boundary marked by the red rectangle; (b, c, d) the Cu vacancy located in the atom plane that is one, two, and three atomic planes away from the grain boundary, respectively. The system energy increases as the separation between the vacancy and grain boundary increases.

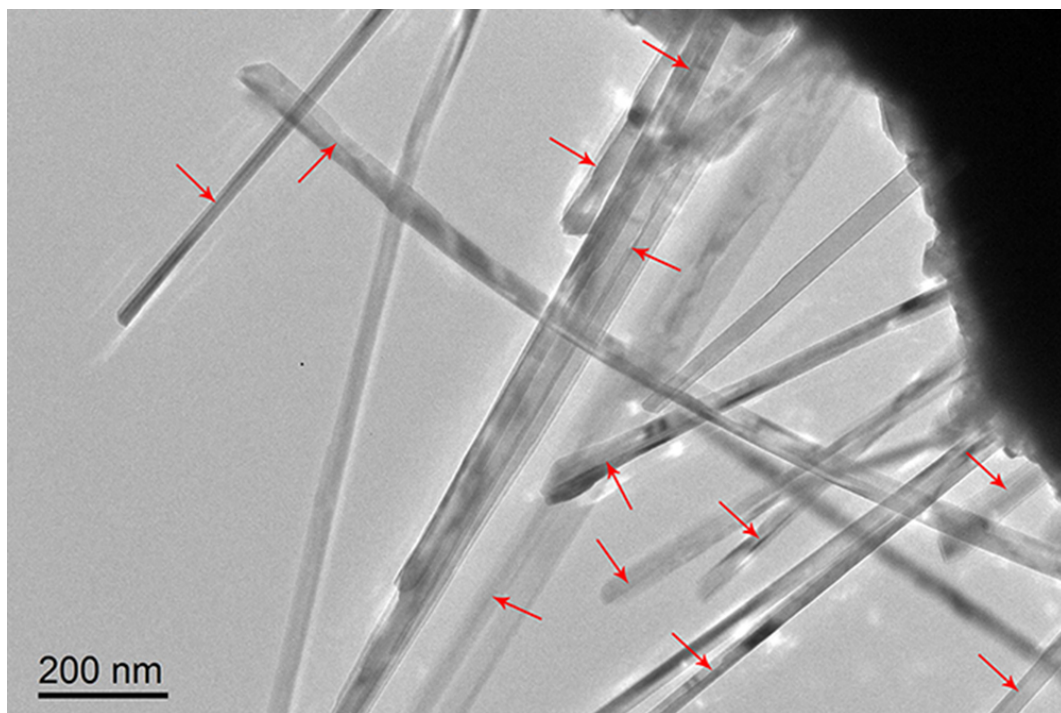


Figure S4. A typical bright-field TEM image of CuO nanowires formed from the thermal oxidation of Cu. The presence of a bicrystal grain boundary is visible for most of the nanowires, as indicated by the red arrows. It is worth mentioning that the bicrystal boundary may become invisible if the grain boundary plane is tilted away from the incident electron beam.

Captions for Supplemental Video

Movie 1: *In situ* TEM observation (electron dose rate of 7.2×10^4 e/(nm²s)) of the growth of a CuO nanowire (diameter of ~ 25 nm) during the oxidation of Cu at T=400 °C and pO₂ ≈ 0.5 Pa. The video is accelerated by a factor of 20 of the real time.

Movie 2: *In situ* TEM observation (electron dose rate of 3.4×10^4 e/(nm²s)) of the growth of a CuO nanowire (diameter of ~ 25 nm) during the oxidation of Cu at T=400 °C and pO₂ ≈ 0.5 Pa. The video is accelerated by a factor of 40 of the real time. Scale bar, 25 nm.

Movie 3: *In situ* TEM observation (electron dose rate of 3.4×10^4 e/(nm²s)) of the growth of a CuO nanowire (diameter of ~ 12 nm) during the oxidation of Cu at T=400 °C and pO₂ ≈ 0.5 Pa. The video is accelerated by a factor of 40 of the real time. Scale bar, 25 nm.

Movie 4: *In situ* TEM observation (electron dose rate of 4.9×10^4 e/(nm²s)) of the tip growth of a bi-crystal CuO nanowire during the oxidation of Cu at 400 °C and ≈ 0.5 Pa of O₂ gas flow. The video is accelerated by a factor of 40 of the real time.

Movie 5: *In situ* TEM observation (electron dose rate of 6.1×10^4 e/(nm²s)) of the nucleation of monoatomic layers at the top-left corner of the tip. The video is accelerated by a factor of 5 of the real time.

Movie 6: *In situ* TEM observation (electron dose rate of 8.3×10^4 e/(nm²s)) of the layer-over-layer, step-flow growth of atomic planes on the tip in the middle region. The video is accelerated by a factor of 5 of the real time.

Movie 7: *In situ* TEM observation (electron dose rate of 6.1×10^4 e/(nm²s)) of the nucleation of atomic layers in the top-right corner region of the nanowire tip and their lateral propagation via

the step-flow growth toward the left side. The video is accelerated by a factor of 5 of the real time.

Movie 8: *In situ* TEM observation (electron dose rate of $5.5 \times 10^4 \text{ e}/(\text{nm}^2\text{s})$) of the oscillatory step-flow growth of a monolayer CuO along the nanowire side facets toward the nanowire root direction during the oxidation of Cu at 400 °C and $\approx 0.5 \text{ Pa}$ of O₂ flow. The video is accelerated by a factor of 5 of the real time.

Movie 9: Animation illustrating the diffusion mechanisms underlying the CuO nanowire growth.